



# A study on structural, optical, and magnetic properties of $\text{MgFe}_2\text{O}_4\text{-BaTiO}_3$ nanocomposites

Mehrnaz Bitaraf<sup>1</sup>, M. E. Ghazi<sup>1,a)</sup> , Morteza Izadifard<sup>1</sup>

<sup>1</sup> Faculty of Physics, Shahrood University of Technology, Shahrood, Iran

<sup>a)</sup> Address all correspondence to this author. e-mail: mghazi@shahroodut.ac.ir

Received: 24 January 2023; accepted: 12 June 2023; published online: 22 June 2023

In this work, the samples of  $\text{MgFe}_2\text{O}_4$  (MFO)<sub>x</sub>- $\text{BaTiO}_3$  (BTO)<sub>(100-x)</sub> ( $x = 10, 20, 30, 40, 50$ ) are synthesized by a sol-gel process. According to the X-ray diffraction data, all composites have the tetragonal phase for BTO, and the spinel phase for MFO. In accordance with FESEM, the ferrite particles become more agglomerated, and have an irregular shape as the  $\text{MgFe}_2\text{O}_4$  concentration increases. The hysteresis loops (M-H) measured at room temperature indicates an increase in the saturation magnetization with an increase in the MFO content. The band gap dependency on the MFO content is also studied using the UV-visible spectra, which show that the band gap energies are in the range of 2.17–2.70 eV. With an increase in MFO, the dielectric constant decreases, and the dielectric tangent loss increases. Also according to the Nyquist plots, as the MFO phase increases in the composites, the diameter of the semicircle also increase indicating the higher resistivity.

## Introduction

Multiferroic materials, which combine ferroelectric and ferromagnetic characteristics, have attracted a lot of attention in the recent years due to their scientific and industrial potentials. They may be employed in a variety of applications including magnetic memory systems, microelectronics, signal processing devices, high-density information storage [1], electrically controlled spintronics [2, 3], nanoelectronics [4], multiple-state magneto-electric memories [5, 6], and magnetic and electric switching [7]; they could also work as magnetic field sensors [1]. An electric field can be used to magnetically polarize some of the multiferroic materials, and a magnetic field can be used to electrically polarize them [8]. Multiferroic composites appear to be a superior alternative to single-phase materials because of their strong magnetoelectric coupling. By combining magnetostrictive and piezoelectric materials, multiferroic composites are produced, applying the interactions between the two phases. When a magnetic-and electric fields are present, the distortion between one of the magnetostrictive and one piezoelectric phase causes the composite materials to exhibit the magnetoelectric effect. This deformation induces stress or strain, which causes a multiferroic interaction between them [9]. The sol-gel, hydrothermal, solid-state reaction, and hybrid techniques are all used to create different multiferroic composite combinations [10–14].

The ferroelectric barium titanate,  $\text{BaTiO}_3$ , belongs to the perovskite structure, and its Curie temperature is at 120 °C, at which point its crystalline structure changes from tetragonal to cubic. The  $\text{Ba}^{2+}$  ion is at the center of the cube. At  $26 \mu\text{C}/\text{cm}^2$ , the ferroelectric  $\text{BaTiO}_3$  will show spontaneous electrical polarization, which may be modified by applying a sufficiently strong electric field in a direction that would induce the change [1]. The  $\text{BaTiO}_3$  powder can be made via solid-state reactions, mechanochemical synthesis, sol-gel, and other processes [15–19]. Its environmental appeal stems from the fact that  $\text{BaTiO}_3$  is lead-free [20]. Because of its outstanding dielectric, ferroelectric, and piezoelectric characteristics,  $\text{BaTiO}_3$  offers a wide range of applications including transducers, thermistors, self-regulating heating systems, and microphones [1, 21]. Because  $\text{MgFe}_2\text{O}_4$  has a high saturation magnetization value, a high Curie temperature, and a high electrical resistivity, it has piqued the curiosity of many researchers compared to other ferrites.  $\text{MgFe}_2\text{O}_4$  is a soft magnetic material with an inverse spinel structure. It also is an n-type semi-conductor material that may be employed as an adsorption device, as well as in sensors and magnetic technologies [22]. Another intriguing feature of  $\text{MgFe}_2\text{O}_4$  is its unusual chemical characteristics and thermal stability, as well as the magnetic properties' reliance on the particle size. Superparamagnetic nanoparticles made of  $\text{MgFe}_2\text{O}_4$  are also possible [22].

Chemical methods were mainly used to synthesize  $\text{MgFe}_2\text{O}_4$  compounds, while physical methods were difficult to implement [23]. Polymeric precursor method [24], co-precipitation [23], sol-gel auto-combustion method [25], high energy milling [26], supercritical hydrothermal reaction [27], mechano-chemistry [28], combustion [29], and microwave hydrothermal method [30] are some of the reported synthesis methods for nanosized  $\text{MgFe}_2\text{O}_4$  particles.

In order to create a system with tailored dielectric, magnetic, magneto-electric, and ferroelectric characteristics, Abraham et al. have studied the encapsulation of non-ferroelectric magnesium ferrite ( $\text{MgFe}_2\text{O}_4$ ) nanoparticles in a ferroelectric shell of  $\text{BaTiO}_3$  [31]. The core-shell interface significantly impacts defect types, attributes, processes, magneto-electric coupling, and the system's electric and magnetic characteristics. The composites have dielectric losses less than 0.10 at 1 MHz (lower than that of the parent materials, MFO, and BTO), which are attributed to the hybrid core-shell structure, and therefore, are ideal for energy storage applications. The magnetic and dielectric characteristics of the composite samples  $x\text{BaTiO}_3-(1-x)\text{MgFe}_2\text{O}_4$  ( $x = 0.35, 0.5, 0.65$ ) were studied as a function of the annealing temperature 950–1150 °C. Saturation magnetization increased upon the increase in annealing temperature up to 1050 °C, and then decreased. It was found that 0.65  $\text{BaTiO}_3$ -0.35  $\text{MgFe}_2\text{O}_4$  composite with an annealing temperature of 1150 °C had a higher dielectric constant. The grain size-dependent polarization is responsible for improving dielectric characteristics in relation to the annealing temperature [9]. As reported for the  $(\text{BaTiO}_3)_{(1-x)}(\text{MgFe}_2\text{O}_4)_x$  samples with  $x = 0.1, 0.2, 0.3$ , and 0.5, by increasing ferrite concentration, the ceramics relative permittivities decrease, while their dissipation factors rise [32]. Additionally, greater permittivities are produced by increasing the sintering temperature up to 1200 °C. In another report on  $(1-x)\text{BaTiO}_3-x\text{MgFe}_2\text{O}_4$  composite ( $x = 0.00, 0.02, 0.04, 0.06$ , and 0.08), the coercivity of the multiferroic composite for  $x = 0.04$  to 0.08 is very small, which is in the range of ~47–53 G [1]. The composite  $(x)\text{MgFe}_2\text{O}_4-(1-x)\text{BaTiO}_3$  ( $x = 0.4, 0.5$ , and 0.6) was also investigated, and the results showed that the composite with  $x = 0.6$  had the highest magnetoelectric coefficient with a value of 50.2 mV/cm Oe at 10 kOe bias magnetic field with a 50 Hz ac magnetic field [8], although the composite of  $\text{BaTiO}_3$  with other ferrites such as  $\text{BaTiO}_3\text{-CoFe}_2\text{O}_4$  [33],  $\text{BaTiO}_3\text{-ZnFe}_2\text{O}_4$  [34],  $\text{BaTiO}_3\text{-NiFe}_2\text{O}_4$  [35], and  $\text{BaTiO}_3\text{-MnFe}_2\text{O}_4$  [36] have been investigated.

The goal of this work was to synthesize the  $\text{MgFe}_2\text{O}_4$   $(\text{MFO})_x\text{-BaTiO}_3$   $(\text{BTO})_{(100-x)}$  ( $x = 10, 20, 30, 40, 50$ ) composites and perform their characterization. Up to now, there are only a few reports on this system especially on optical investigation. Various weight percentages of MFO and BTO nano-powders were used to create MFO-BTO nanocomposites using a modified sol-gel method for BTO and a self-combustion method for

MFO. Investigations were conducted on the prepared composite to determine its structural, optical, dielectric, magnetic, and electrical conduction characteristics. To the best of our knowledge, there was no comprehensive report for this composite's dielectric properties such as the imaginary part of the dielectric constant, electric modulus, and Nyquist plots.

## Characterization

Using a Field Emission Scanning Electron Microscope (FESEM: Sigma 300-HV, Zeiss, Germany), the surface morphology of all nanocomposites was studied. The XRD patterns of the produced materials were captured using a D8-Advance Bruker AXS diffractometer using  $\text{Cu K}\alpha_1$  radiation with a wavelength of 0.15406 nm. The detection of optical absorption was carried out using a Shimadzu UV-visible (UV1800, Shimadzu, Japan) spectrophotometer (in the scanning wavelength range of 190–1100 nm). To ascertain the samples dielectric properties, a LCR-meter (HIOKI IM3536, Japan) was employed. A vibrating sample magnetometer (VSM) with a maximum magnetic field of 0.8 T was used to record magnetic hysteresis (M-H) loops for samples (Taiwan's Weistron VSM1100). Figure 1 shows a schematic representation of the preparation method for the BTO, MFO, and BTO-MFO nanocomposites.

## Results and discussion

### X-ray diffraction (XRD)

Figure 2(a) depicts the X-ray diffraction patterns of the prepared MFO, BTO, and  $(\text{MFO})_x\text{-BTO}_{(100-x)}$  ( $x = 10, 20, 30, 40, 50$ ) samples. In order to validate the phase, the BTO and MFO XRD patterns were compared with JCPD 00-005-0626 and 01-073-1720, respectively. The perovskite  $\text{BaTiO}_3$  (space group  $P4/mmm$ ) and spinel  $\text{MgFe}_2\text{O}_4$  (space group  $Fd-3m$ ) are the two primary phases that make up the XRD patterns of the composites, along with a few more minor impurity phases. The composite systems display both parent phases, as seen. In the XRD pattern for MFO-BTO composite, the planes (100), (110), (111), (200), (210), (211), and (202) are those that match the tetragonal structure of  $\text{BaTiO}_3$ , whereas the planes (220), (311), (400), (422), (511), and (440) correspond to the of  $\text{MgFe}_2\text{O}_4$  phase [31]. In addition to these phases, a few small peaks corresponding to the  $\text{Ba}_4\text{Ti}_2\text{O}_{27}$  (JCPDS 00-044-0013) secondary phase is found in  $\text{BaTiO}_3$ . The presence of a minor impurity phase has been reported by other authors [37–39]. Additionally, Table 1 includes the phase fractions for each sample, which were determined. The results demonstrated that, with the exception of the 10MFO-90BTO sample, the phase fractions were almost identical to the weight percentages. As the small crystallite size and strain are two main sources of the peak broadening, so the Williamson-Hall (W-H) plot method was used to separate these

two effects. The Williamson-Hall (W-H) equation (Eq. 1) was used to determine the strain and average nano-crystallite size of the obtained samples [40].

$$\beta \cos \theta = \frac{k\lambda}{D} + 4\varepsilon \sin \theta \quad (1)$$

where  $\varepsilon$  is the lattice strain,  $\lambda$  is the X-ray wavelength,  $\beta$  is the full-width at half-maximum, and  $\theta$  is the Bragg angle of the diffraction peaks. Figure 3(a-e) displays the plot of the  $\beta \cos \theta$  versus  $4 \sin \theta$  for the  $(\text{MFO})_x-(\text{BTO})_{(100-x)}$  ( $x = 10, 20, 30, 40, 50$ ) nanocomposites. It is important to note that it is an approximation and may not always provide accurate results. The (100), (110), (200), (210), (211), (111) reflections for the BTO phase and (220), (311), (400), (440), (511) reflections for the MFO phase were chosen to the W-H plots depending on peak intensity in the corresponding pattern. Due to the low weight percentage of MFO in the 10MFO-90BTO sample, the MFO phase was not observed in the XRD pattern.

The lattice constants ( $a = b$  and  $c$ ) of the tetragonal structure and the lattice constants ( $a = b = c$ ) of the cubic structure were obtained using the following equations [41]:

$$\frac{1}{d^2} = \frac{h^2 + k^2}{a^2} + \frac{l^2}{c^2} \quad (2)$$

$$\frac{1}{d^2} = \frac{h^2 + k^2 + l^2}{a^2} \quad (3)$$

where  $h, k,$  and  $l$  indicate the Miller's indices of the reflecting planes, and  $d$  is the distance between the  $hkl$  planes. Figure 2(b) displays the crystallite size values for both phases in composites. The average crystallite size and lattice properties of the two phases are summarized in Table 1. Zolkepli et al. reported the variation of the lattice parameters  $a$  and  $c$  with the weight fraction [1], and mentioned that although there was not much change in the lattice parameters, the tetragonality of  $\text{BaTiO}_3$  decreased when  $\text{MgFe}_2\text{O}_4$  was added consistent with our result. As Fig. 2(b) shows, by increasing the amount of MFO in the nanocomposites, the crystallite size of the magnesium ferrite phase grows, and the crystallite size of BTO phase decreases. It seems that increasing the MFO amount in the nanocomposites causes stress on the BTO crystallites during the sintering process [42]. These two phases can produce the magnetostriction and piezoelectric effects required for multiferroic coupling in the presence of a magnetic field.

### FE-SEM analysis

Figure 4 shows the particle size distribution curves and FESEM images of the produced samples. Increasing  $\text{MgFe}_2\text{O}_4$  content appears to result in a small reduction in grain sizes. On the other hand, as the  $\text{MgFe}_2\text{O}_4$  percentage increases, the ferrite particles tend to become more agglomerated and irregularly shaped. Agglomeration of the particles can be attributed to the magneto-static interactions between them [9, 32].

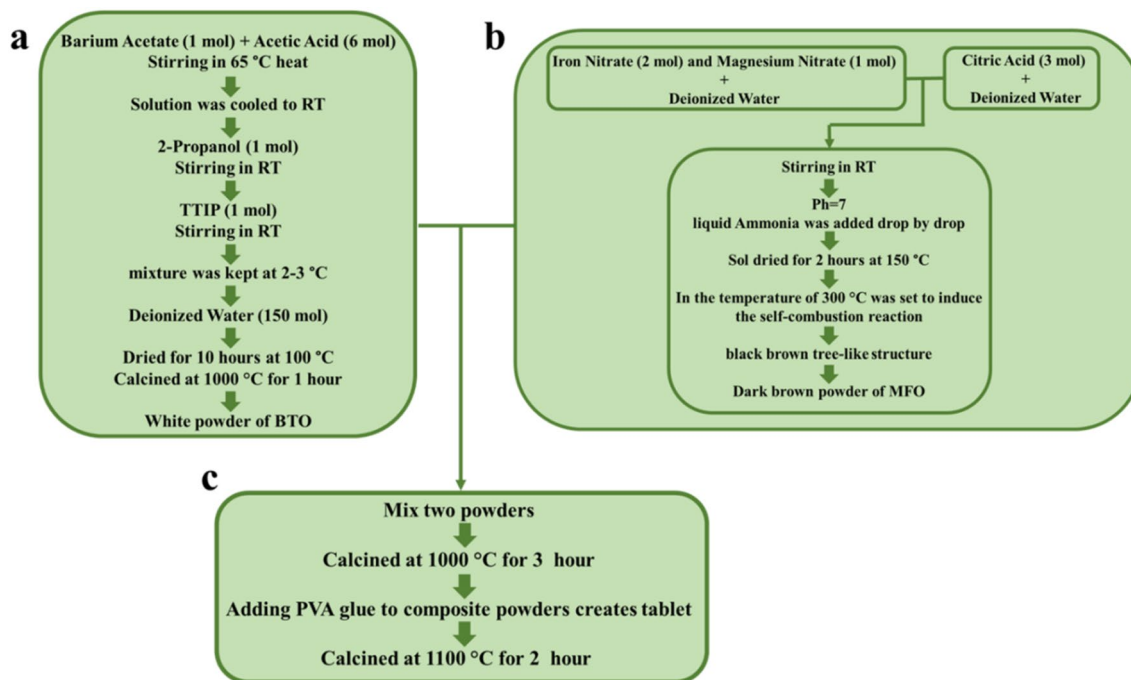


**Figure 1:** Schematic flow chart of (a) sol-gel synthesis of BTO, (b) self-combustion reaction synthesis of MFO, and (c) BTO-MFO nanocomposites and tablet.

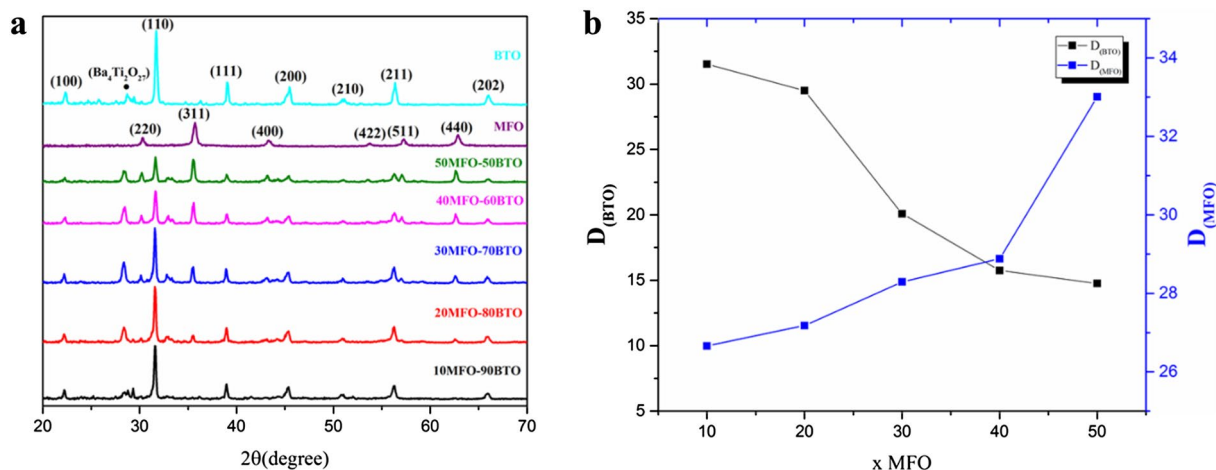


**Figure 2:** (a) XRD patterns for BTO, MFO, and  $(\text{MFO})_x-(\text{BTO})_{(100-x)}$  ( $x = 10, 20, 30, 40, 50$ ) nanocomposites. (b) Crystallite size of barium titanate and magnesium ferrite in the  $(\text{MFO})_x-(\text{BTO})_{(100-x)}$  ( $x = 10, 20, 30, 40, 50$ ) nanocomposites.

**TABLE 1:** Lattice constants and crystallite sizes (D), strain, and phase fraction.

Sample	Phase	Phase fraction	Lattice constants (nm)	Crystallite size (nm)	Strain
10MFO-90BTO	BTO	97.14	$a = 3.987, c = 4.05$	31.51	0.006
	MFO	2.85	8.6	26.66	0.008
20MFO-80BTO	BTO	82.96	$a = 4.003, c = 4.054$	29.5	0.005
	MFO	17.03	$a = 8.395$	27.18	0.003
30MFO-70BTO	BTO	76.04	$a = 4.010, c = 3.970$	20.09	0.004
	MFO	23.95	$a = 8.384$	28.29	0.003
40MFO-60BTO	BTO	66.65	$a = 4.019, c = 3.979$	15.75	0.003
	MFO	33.34	$a = 8.369$	28.88	0.003
50MFO-50BTO	BTO	49.79	$a = 4.007, c = 3.981$	14.75	0.003
	MFO	50.2	$a = 8.365$	33.01	0.004

The obtained average particle size for all samples is around 150 nm, as seen in the size distribution histograms (Fig. 4), while the average particle size for the  $x = 20$  sample is two times larger (using the Digimazer software). When the particle size is compared with the size of the average crystallite size in Table 1, it is clear that each particle is made up of many crystallites. As the  $\text{MgFe}_2\text{O}_4$  concentration increases, the ferrite particles become more agglomerated, and have an uneven form.

To provide a better understanding of the obtained results, the differences between the crystallite size calculated from the XRD data and the particle size measured by SEM is necessary. The particle is created by joining a number of crystallites with specific lattice spacing “d”. Crystallite size is the smallest unit and is measured as the size of coherently diffracting domains of material. So a particle is made of one or in most cases more crystallites [43].

### Optical study

The reflectance spectra within the wavelength range of 400–1100 nm were used to investigate the optical characteristics of

the tablets created from the manufactured powders. The recorded spectra are shown in Fig. 5(a). The Tauc relation was used to calculate the direct optical band gap energies [44]:

$$(F(R)h\nu)^2 = A(h\nu - E_g) \quad (4)$$

where  $F(R)$  is the Kubelka–Munk function, and  $R$  is the reflectance.

$$F(R) = \frac{(1 - R)^2}{2R} \quad (5)$$

The linear portion of the  $(F(R)h\nu)^2$  against  $h\nu$  curves was extrapolated to obtain the bandgap values, as shown in Fig. 5(b) [45].

It is worth mentioning that when the crystal is defect free, inter-band transition in  $(F(R)h\nu)^2$  versus  $h\nu$  curve is sharp. But when defects are present in the crystal, the transition starts gradually due to the band-tail. So when the  $(F(R)h\nu)^2$  versus  $h\nu$  curves for samples are plotted together, the curves near to the band gap values of samples may cross each other.

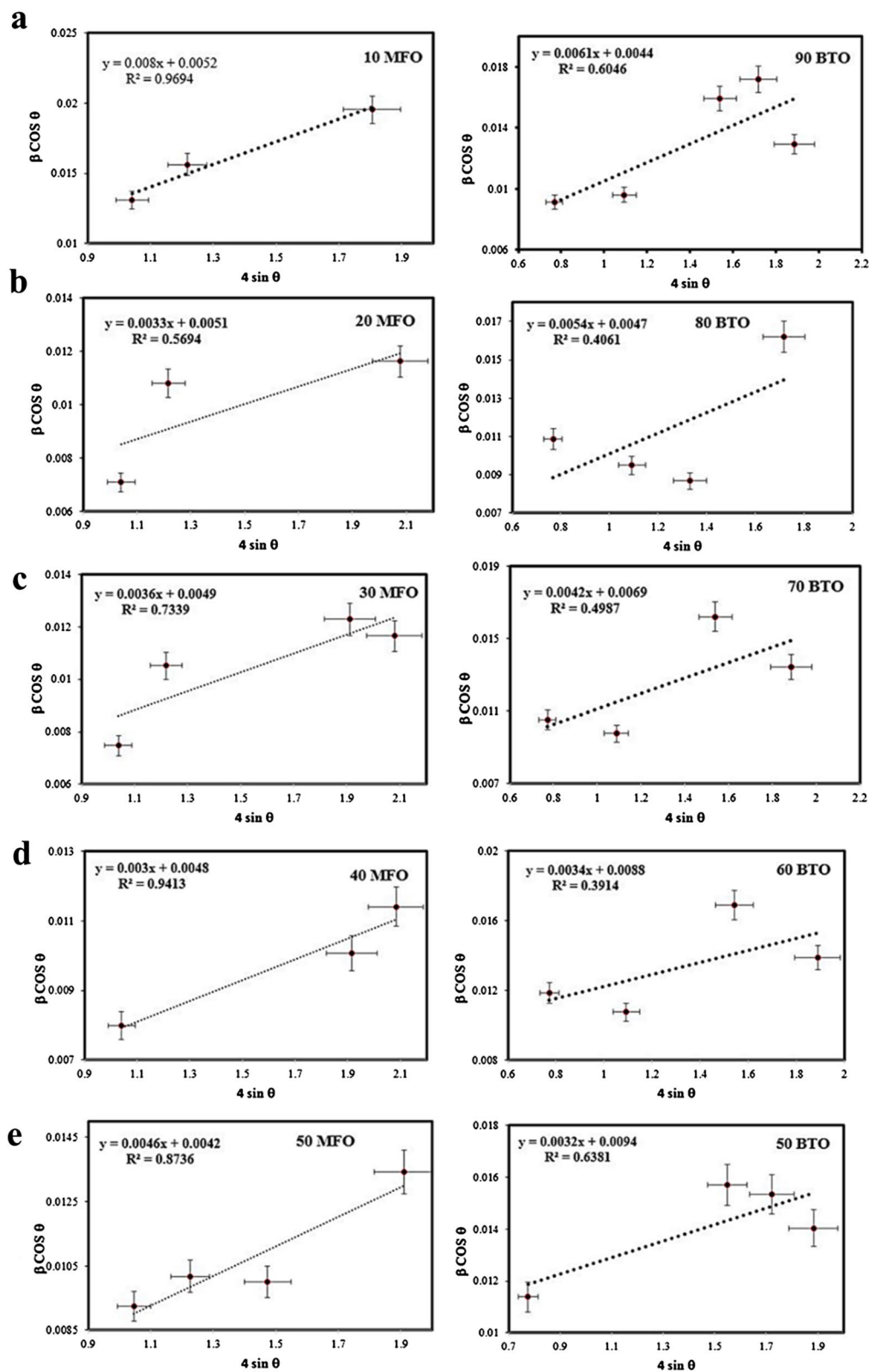
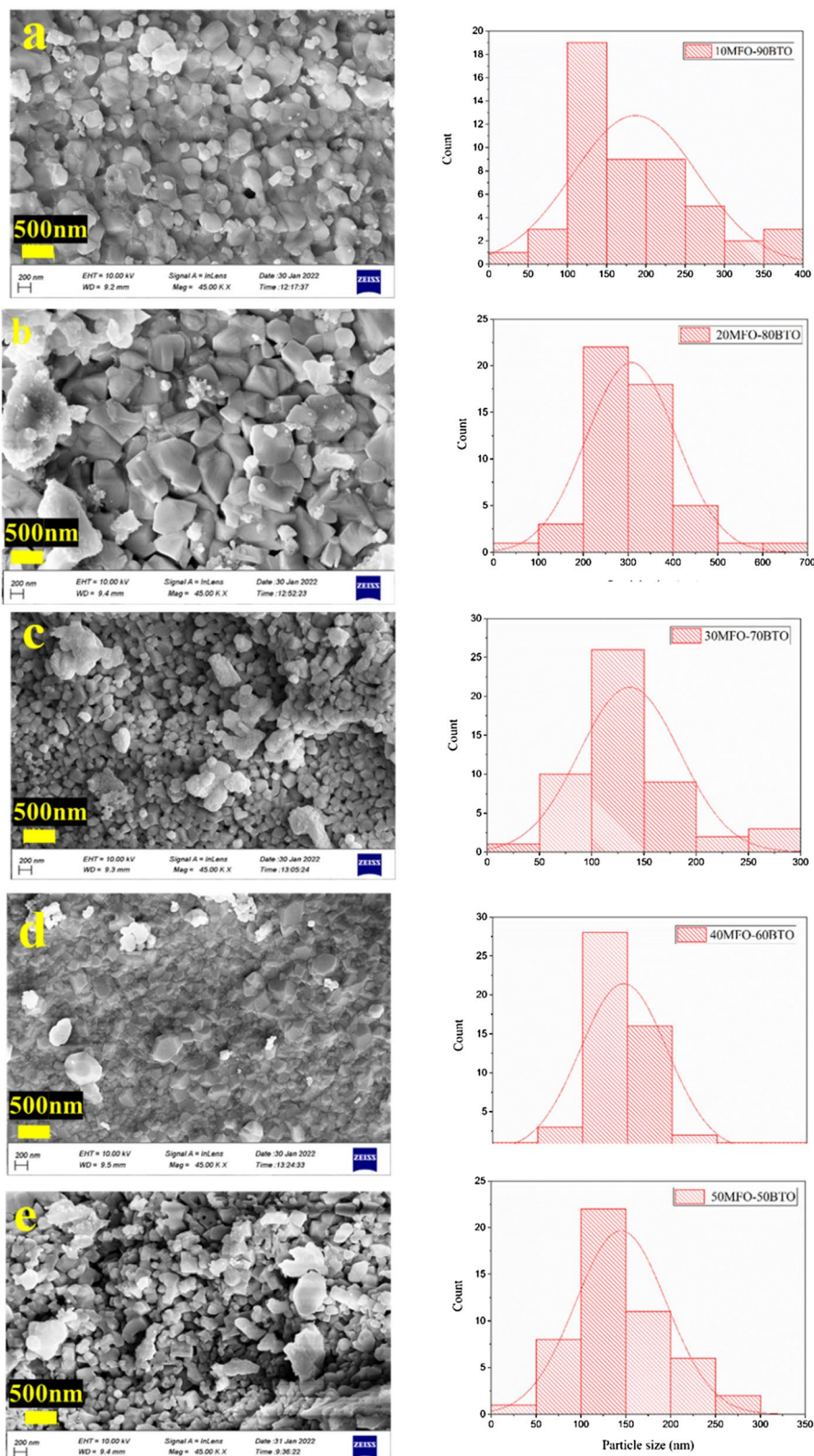


**Figure 3:** Williamson-Hall plot of  $\beta\cos\theta$  against  $4\sin\theta$  for the  $(\text{MFO})_x-(\text{BTO})_{(100-x)}$  (a)  $x=10$ , (b)  $x=20$ , (c)  $x=30$ , (d)  $x=40$ , (e)  $x=50$  nanocomposites.

The band gaps for the  $(\text{MFO})_x-(\text{BTO})_{(100-x)}$  ( $x = 10, 20, 30, 40, 50$ ) composites were obtained from Fig. 5(b), and plotted in Fig. 5(c). The Fig. 5(c) shows that as the concentration

of the MFO increases, the band gap decreases. This could be due to the smaller bandgap value of MFO compared to the barium titanate. Actually, reported values of the band gap

**Figure 4:** FESEM images of  $(\text{MFO})_x-(\text{BTO})_{(100-x)}$  (a)  $x = 10$ , (b)  $x = 20$ , (c)  $x = 30$ , (d)  $x = 40$ , (e)  $x = 50$  nano-composites. Histograms for the particle size distributions (right).



for MFO is around 2.18 eV [46] and the band gap value of the BTO is greater than 3 eV [47]. The composites bandgaps are approximately 2.5–2.9 eV, consistent with the Vegard’s law [48].

The composite fundamental band gap should be between these two values depending on the two phases ration according to Vegard’s law [48]. The other ranges observed in Fig. 5(b) may be produced from indirect transition or transition associated to the defects. So the fitted range indicated in Fig. 5 was chosen to obtain the band gap value.

The composite band gap energy, therefore, reduces as the ferrite phase is enhanced. This shows that it may be possible to change the band gap for a range of energies by just modifying the molar ratio of phases. A band gap value of 2.6 eV has been reported for the BTO-MFO core-shell structure [49].

### Magnetic measurements

Figure 6(a) depicts the hysteresis loops for the MFO and  $(\text{MFO})_x-(\text{BTO})_{(100-x)}$  ( $x = 10, 20, 30, 40, 50$ ) nanoparticles at room temperature. It proves the presence of an ordered magnetic structure in the mixed spinel-perovskite system. Due to the ferrite phase of  $\text{MgFe}_2\text{O}_4$ , the composite samples displayed the features of soft magnetic materials and suitability for device applications [8]. Table 2 displays the magnetic parameters that were derived from the hysteresis loops. It is evident that as the MFO concentration increases, so do the  $M_s$  and  $M_r$  values for the composite [Fig. 6(b)]. The increase in these parameters upon an increase in the MFO phase, may be explained by two factors. One is crystallite size enhancement in the magnetic phase [see Fig. 2(b)] and the second one is increasing MFO amount, which leads to continuous exchange interaction among magnetic domains in the ferrimagnetic phase, thus raising the net

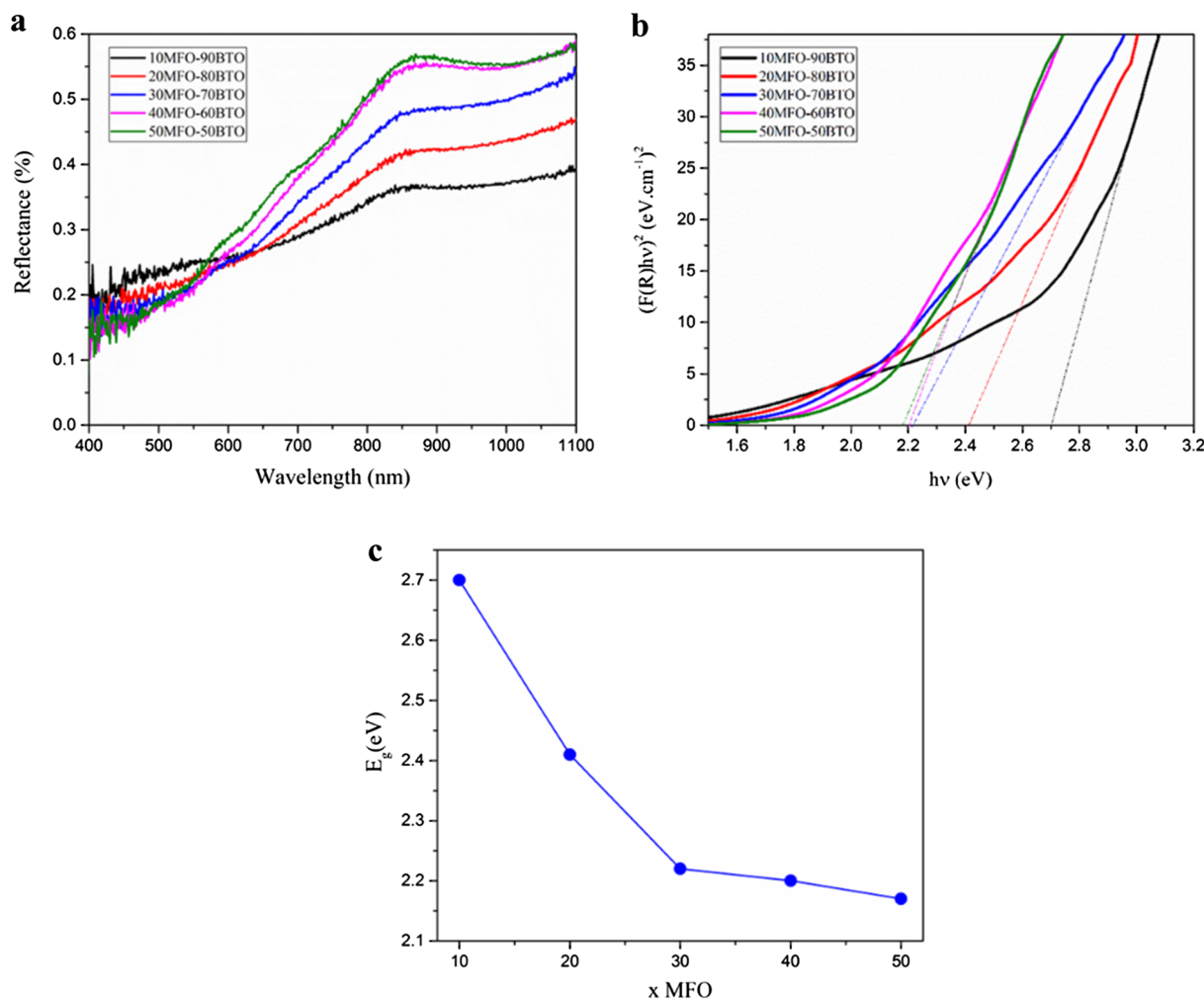


**Figure 5:** (a) Reflectance versus wavelength spectra. (b) Variation of  $(F(R)hv)^2$  versus  $hv$ . (c) Variation of the bandgap ( $E_g$ ) in  $(\text{MFO})_x-(\text{BTO})_{(100-x)}$  ( $x = 10, 20, 30, 40, 50$ ) nanocomposites.

magnetic moment as the BaTiO<sub>3</sub> is a non-magnetic material [1]. The multiferroic composite has a low coercivity, which ranges from 72 to 79 Oe for x = 10 to 50.

The M<sub>s</sub> and M<sub>r</sub> values of the nanocomposite BTO-MFO are smaller than the corresponding values for MFO, which may be explained by the presence of the non-magnetic BTO phase in the overall volume of the composite [8]. Figure 6(a) shows that at a field greater than 2000 Oe, the magnetization starts to saturate. The increase in magnetization for the samples with higher value of MFO indicates that the magnetic characteristics are influenced by the quantity of the magnetic material [1].

Synthesis of (BTO)<sub>x</sub>-(MFO)<sub>(1-x)</sub> bulk composites with x = 0.35, 0.5, and 0.65 was reported by Tadi et al., and the result showed that the 0.35BTO + 0.65MFO composite had the highest saturation magnetization value (about 19 emu/g) compared to the x = 0.65 (about 9 emu/g) [9]. This reduction is attributed to the discontinuous exchange contact between the magnetic domains. Thus the net magnetization value tended to decrease as the ferromagnetic phase (MFO phase) was reduced. According to the Köferstein et al. report, the (BaTiO<sub>3</sub>)<sub>1-x</sub>-(MgFe<sub>2</sub>O<sub>4</sub>)<sub>x</sub> composite powders with x = 0.1, 0.2, 0.3, and 0.5 treated at 1000 °C and higher demonstrated ferrimagnetic behavior with maximum coercivity value of 63 Oe at 300 K [32]. Zolkepli et al. reported that the coercivity of the multiferroic composite (1-x) BaTiO<sub>3</sub>-xMgFe<sub>2</sub>O<sub>4</sub> (x = 0.04 to 0.08) was in the range of 47–53 G, which was extremely low [1]. Table 2 lists the obtained values of the squareness ratio SQR, which is defined as M<sub>r</sub>/M<sub>s</sub> and computed from our measured hysteresis data. When the SQR is equal to or greater than 0.5, the nanoparticles are thought to be in a single magnetic domain (SMD). However, the nanoparticles are believed to be in multi-magnetic domains if SQR is less than 0.5 (MMD) [50, 51]. Our results for SQR are consistent with the work of Zolkepli et al. [1] and SQR is less than 0.5. Tan et al. have

concluded that the composite with the greatest ferrite concentration, 0.6MgFe<sub>2</sub>O<sub>4</sub>-0.4BaTiO<sub>3</sub>, has saturated M<sub>s</sub> and remnant M<sub>r</sub> magnetization values of 6.27 and 1.63 emu/g, respectively, which are much smaller than our result (Table 2) [8].

Calculating important magnetic parameters like the magneton number (n<sub>B</sub>) may be done using the saturation magnetization value. The following equation was used to compute the magneton number for all samples [52]:

$$n_B = \frac{MM_s}{N_A \mu_B} \quad (6)$$

where M denotes the molecular weight, N<sub>A</sub> is the Avogadro number, and μ<sub>B</sub> indicates the Bohr magneton. The n<sub>B</sub> values for the prepared samples are shown in Table 2, demonstrating that the magneton number (n<sub>B</sub>) rises as the MFO content does. The increase in the exchange contacts between Mg and Ba cations, which ultimately results in an increase in the net magnetization and magnetic moment per formula unit, is responsible for this rise in the magneton number [53].

**TABLE 2:** Magnetic parameters for the nanocomposites (MFO)<sub>x</sub>-(BTO)<sub>(100-x)</sub> (x = 10, 20, 30, 40, 50) and MFO.

Sample	M <sub>s</sub> (emu/g)	M <sub>r</sub> (emu/g)	H <sub>c</sub> (Oe)	M <sub>r</sub> /M <sub>s</sub>	n <sub>B</sub>
MFO	18.089	6.527	175.568	0.36	0.64
10MFO-90BTO	0.9725	0.218	78.248	0.224	0.04
20MFO-80BTO	2.96	0.668	72.726	0.225	0.12
30MFO-70BTO	6.432	1.468	79.078	0.228	0.25
40MFO-60BTO	10.558	2.346	75.104	0.222	0.41
50MFO-50BTO	13.15	3.027	79.841	0.23	0.5

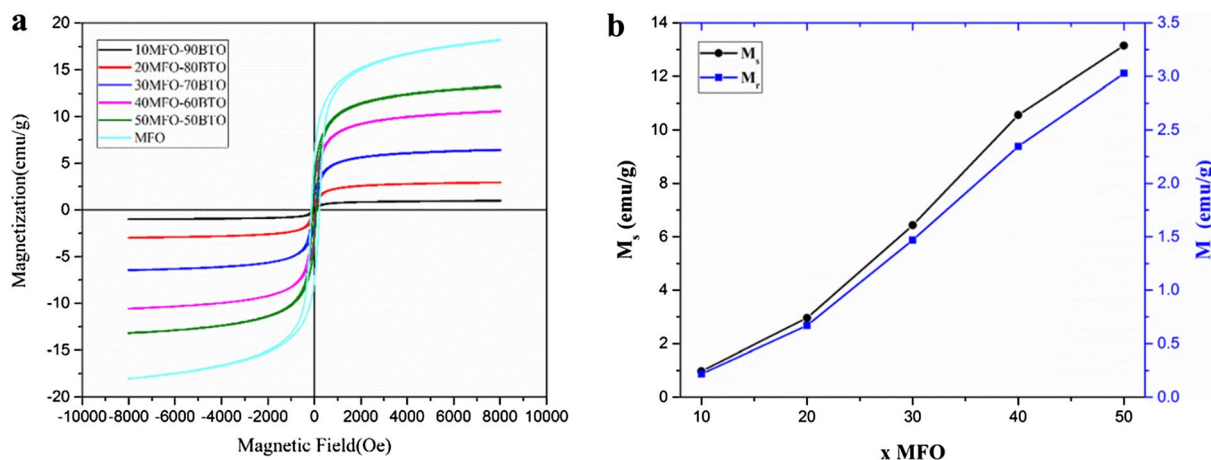


**Figure 6:** (a) Hysteresis loops for the (MFO)<sub>x</sub>-(BTO)<sub>(100-x)</sub> (x = 10, 20, 30, 40, 50) nanocomposites. (b) Variations of M<sub>r</sub> and M<sub>s</sub> values with MFO content (x) in the composite.



## Dielectric study

The produced powders were utilized to create the tablets, which were then used to analyze the samples dielectric characteristics. Ag was coated on the tablet's top and bottom in order to create capacitors. The sample capacitance was measured throughout a frequency range, and the relative dielectric constant was then calculated using Eq. 7 [54].

$$\epsilon_r = \frac{Cd}{\epsilon_0 A} \quad (7)$$

where A is the cross-section area, d is the tablet thickness, C is the capacitance,  $\epsilon_r$  is the relative dielectric constant, and  $\epsilon_0$  is the free space permittivity ( $8.85 \times 10^{-12}$  F/m). Figure 7(a) shows variation of the dielectric constant with frequency in semi-logarithmic scale for prepared samples at room temperature. The inset curve displays the dielectric constant versus frequency for the x = 10 sample that has a higher value of the  $\epsilon_r$ . The dielectric constant appeared to drop as the ferroelectric phase was shrunk (from x = 10 to 50), proving that the dielectric characteristic is dependent on the concentration of BaTiO<sub>3</sub> in the samples. Due to the fact that ferrites are often electrically leaky by nature, increasing ferroelectric concentration correlates to a higher dielectric constant and reduced loss [8]. The number of dipoles contributing to the polarization of the dielectric material reduces as the ferromagnetic phase increases. It has been reported that dielectric characteristics are correlated with the chemical composition, synthesis methods, grain-level conduction processes, annealing temperatures, and grain size [55]. The movement of electrons between various cations weakens the polarization process described by Maxwell–Wagner polarization, which is why the dielectric constant decreases as frequency increases [9, 56, 57]. The measured dielectric constant for samples is consistent with the previously published values [58, 59].

Tadi et al. [60] stated that 0.5BaTiO<sub>3</sub>–0.5MgFe<sub>2</sub>O<sub>4</sub> treated at 1050 °C had a dielectric constant of about 46. Reduction of the dielectric constant also reported that when the ferroelectric phase was reduced (from x = 0.65 to 0.35), demonstrating the reliance of the dielectric characteristic on the amount of BaTiO<sub>3</sub> present in the samples [9]. The work by Köferstein et al. showed the values for the dielectric constants for (BaTiO<sub>3</sub>)<sub>(1-x)</sub>–(MgFe<sub>2</sub>O<sub>4</sub>)<sub>(x)</sub> (x = 0.1, 0.2, 0.3, and 0.5) composites were nearly equal [32], and did not vary all that much between 0.5 MHz and 13 MHz. This behavior is consistent with our data for the x = 40, 50 samples.

The frequency dependence of the complex dielectric permittivity is written as [61]:

$$\epsilon^* = \epsilon' - i\epsilon'' \quad (8)$$

where  $\epsilon'$  is the real part of dielectric constant and the imaginary part denoted as  $\epsilon''$ . The imaginary part representing the amount of energy loss while an electric field is applied and was calculated

from the dielectric loss tangent ( $\tan \delta$ ) and  $\epsilon'$  by the following relation [62]:

$$\epsilon'' = \epsilon' \tan \delta \quad (9)$$

$\epsilon'$  and  $\epsilon''$  decrease almost linearly with increased frequency [61]. Dielectric loss is the main cause of electromagnetic energy dissipation. It is well documented that polarization relaxation and conduction loss are the two main contributions to dielectric loss [63]. Figure 7(b) shows the normal behavior of a dielectric material, a decrease in the imaginary part  $\epsilon''$  with increased frequency due to the presence of distinct polarization processes [62].

In Fig. 7(c), the dielectric loss,  $\tan \delta$ , versus frequency is shown. The  $\tan \delta$  values for these composites, like  $\epsilon_r$ , decrease as frequency increases. Also it was found that the dielectric tangent loss increased as the MgFe<sub>2</sub>O<sub>4</sub> concentration increased. To meet the requirements for microwave applications, dielectric losses must be sufficiently low. The produced composites have a dielectric loss between 0.1 and 0.2 at 1 MHz frequency [Fig. 7(c)], make them nearly ideal for energy storage applications. It has been stated that presence of pores in the samples may effect on the energy dissipation mechanism and the dielectric loss [64]. When a sample contains more pores, the dielectric loss increases due to increased interfacial areas between the composite materials. So in addition to the phase concentration of two species in composite, the porosity [64], imperfections in the crystal lattice and grain boundaries [65] of the sample may affect on the dielectric properties and causes overlapping of some curves with each other at some frequency range. A low dielectric loss tangent and a high dielectric constant are two examples of the material's good dielectric properties. The shape, size, and dielectric constants of the materials that make up the composites affect the application capabilities [31].

Ac conductivity measurement is an important tool for studying the ionic transport properties of materials. It was obtained using the following relation [66]:

$$\sigma = \omega \epsilon_0 \epsilon'' = 2\pi f \epsilon_0 \epsilon'' \quad (10)$$

where f is the frequency of the applied field,  $\epsilon''$  is the imaginary part of the dielectric constant,  $\omega = 2\pi f$  is the angular frequency and  $\epsilon_0$  is the permittivity of free space.

Figure 7(d) depicts the frequency dependence of conductivity in the 10<sup>2</sup>–10<sup>7</sup> Hz frequency range for the (MFO)<sub>x</sub>–(BTO)<sub>(100-x)</sub> samples. The conductivity remains constant and low up to around 10<sup>5</sup> Hz, and then increases sharply for all samples. The frequency threshold for this increase depends on the MFO concentration. Furthermore, as the amount of ferrite in the composite increases, the conductivity goes down. At high frequencies, a potent conduction mechanism between the ions Ti<sup>4+</sup>/Ti<sup>3+</sup> and Fe<sup>3+</sup>/Fe<sup>2+</sup> may be produced [67]. Abraham et al. [31] show that the conductivity rises with frequency, and that tiny polaron hopping is responsible for the conduction phenomena in these composites.

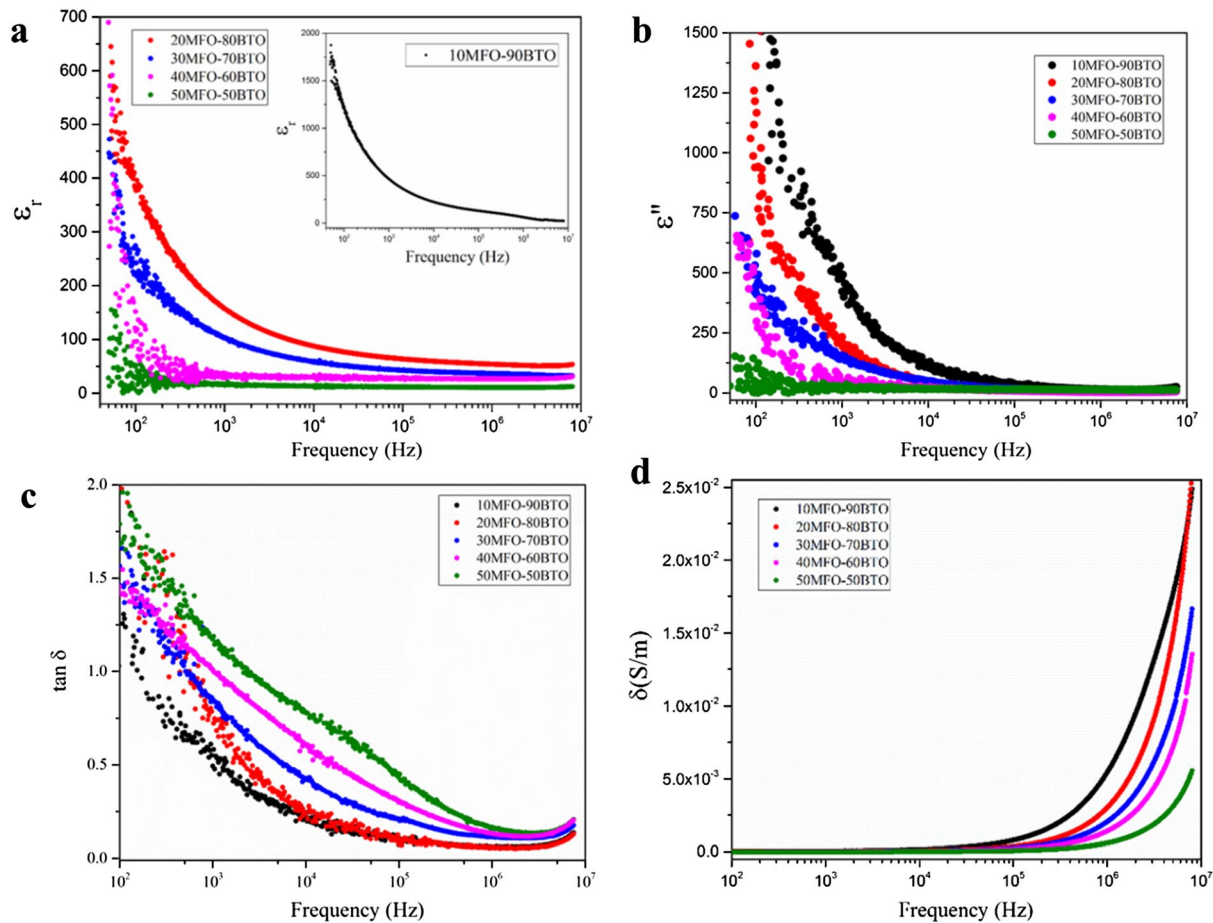


**Figure 7:** Dielectric constant (a) and the imaginary part of the dielectric constant (b) versus frequency for (MFO)<sub>x</sub>-(BTO)<sub>(100-x)</sub> (x = 10, 20, 30, 40, 50) composites. (c) Variation of dielectric loss with applied frequency for (MFO)<sub>x</sub>-(BTO)<sub>(100-x)</sub> BTO (x = 10, 20, 30, 40, 50) composites. (d) Conductivity versus frequency for (MFO)<sub>x</sub>-(BTO)<sub>(100-x)</sub> (x = 10, 20, 30, 40, 50) composites.

The dielectric modulus is related to the complex permittivity and is given by [68]:

$$M^* = M' + iM'' = \frac{\epsilon'}{\epsilon' + \epsilon''} + i \frac{\epsilon''}{\epsilon' + \epsilon''} \quad (11)$$

The variation of the  $M''$  as a function of frequency for (MFO)<sub>x</sub>-(BTO)<sub>(100-x)</sub> samples shown in Fig. 8(a). refers to the presence of an asymmetric peak that confirms a non-Debye type relaxation[69]. The figure shows that the peak position moves to higher frequencies with increased MFO content. In a  $M''$  versus frequency diagram, a peak appearing at a low frequency indicates the grain boundary influence on the relaxation time. So at low MFO content, grain boundaries contribute to charge carrier's movement and as the MFO content increases, grains play more roles in charge movement.

It has been proposed that the conduction is through the long-range hopping between neighboring sites at low frequency while at high frequency, the charge carriers undergo localized motion through short-range hopping in spatial confinement in

their potential wells at the grains [62]. Therefore, the shift in peak position observed in Fig. 8(a) shows a transition from long-range hopping to short-range hopping. According to the relaxation time formula,  $\tau = \frac{1}{2\pi f_{max}}$  [68], a lower amount of relaxation time observed in x = 50 sample as compared with the other samples indicates lower mobility of charge carriers in this sample which is consistent with our conductivity result [Fig. 7(d)] [70].

A well-known and useful tool for fully understanding the electrical properties of materials is the complex impedance spectrum. The complex impedance  $Z^*$  is given by the following relation[68]:

$$Z^* = Z' + iZ'' = \frac{\epsilon''}{\omega c(\epsilon' + \epsilon'')} - i \frac{\epsilon'}{\omega c(\epsilon' + \epsilon'')} \quad (12)$$

The  $Z''$  vs.  $Z'$  plots (known as the Nyquist plots or Cole-Cole plots) for the samples are shown in Fig. 8(b).

All  $Z''$  vs.  $Z'$  plots normally exhibit two semicircular arcs. The first semicircular arc is due to grain while the second one is

due to grain boundaries contribution on the conductivity. The radius of both semicircles is proportional to the resistivity of the samples: the smaller the radius, the lower the resistivity. Figure 8(b) shows the Nyquist diagrams of all the samples, in which the second larger semicircle appears, due to the grain boundary contribution to the impedance. As the MFO phase increases in composites, the diameter of this semicircle increases. Increasing the diameter indicates higher resistivity.

## Conclusion

This work investigated and synthesized the BaTiO<sub>3</sub> and MgFe<sub>2</sub>O<sub>4</sub> composites with the formula (MFO)<sub>x</sub>–(BTO)<sub>(100–x)</sub> (x = 10, 20, 30, 40, 50) using the sol–gel combustion and sol–gel techniques. The emergence of the tetragonal phase for BTO and the spinel phase for MFO in all samples was confirmed by the X-ray diffraction data. As the amount of BTO in the nanocomposites dropped, the crystallite size of BTO fell but the crystallite size of MFO grew. The ferrite particles became increasingly agglomerated, and had an irregular shape as the MFO concentration rises. When the MFO concentration in the composite increased, the bandgap also decreased, from 2.70 eV for x = 10 to 2.17 eV for x = 50. The M vs. H hysteresis loop indicated that adding MFO gave the composite soft magnetic characteristics. The coercive field was small (from 72.72 Oe to 79.84 Oe). In addition, the magnetization rose when the MFO concentration went up from 0.9725 emu.g<sup>–1</sup> for x = 10 to 13.150 emu.g<sup>–1</sup> for x = 50. The dielectric constant (real and imaginary) of (MFO)<sub>x</sub>–(BTO)<sub>(100–x)</sub> composites decreased as ferrite content increased, while dissipation factors increased. The conductivity measurements revealed that it was constant at low to moderate frequencies, and increased sharply at high

frequencies. The result obtained from the dielectric modulus showed the presence of an asymmetric peak that confirms a non-Debye-type relaxation. The lower amount of relaxation time with increase in MFO content indicates lower mobility of charge carriers in the sample with x = 50 as compared with the other samples.

## Materials and methods

The modified sol–gel process was used to create barium titanate (BTO) nanoparticle. Barium acetate (C<sub>4</sub>H<sub>6</sub>BaO<sub>4</sub>, Merck (99%)), 2-propanol (CH<sub>3</sub>CH(OH)CH<sub>3</sub>, Merck (99%)), titanium isopropoxide (TTIP) (Ti(OCH(CH<sub>3</sub>)<sub>2</sub>)<sub>4</sub>, Merck (97%)), acetic acid (CH<sub>3</sub>COOH, Merck (99%)), and deionized water were used as the raw materials. In the optimal sol formulation, the ratios of the acetic acid, barium acetate, titanium isopropoxide, 2-propanol, and deionized water were 6:1:1:1:150, respectively. The following procedure was used to create the compound: barium acetate was first dissolved in acetic acid at temperature 65 °C, after which the solution was cooled to room temperature, and 2-propanol was added to the solution. The subsequent step involves the addition of TTIP, which results in partial hydrolysis. The mixture was kept at 2–3 °C, while the deionized water was added to it simultaneously. Using a magnetic stirrer, the liquid was agitated during the whole sol preparation process. After developing a transparent, colorless sol, it was eventually dried for 10 h at 100 °C. For the purpose of creating white barium titanate powder, the dried gel was calcined at 1000 °C for 1 h. To prepare magnesium ferrite (MFO) nanoparticles, the self-combustion reaction method was adopted. Magnesium ferrite (Mg(NO<sub>3</sub>)<sub>2</sub>·6H<sub>2</sub>O, Merck (99%)), iron nitrate (Fe(NO<sub>3</sub>)<sub>3</sub>·9H<sub>2</sub>O, Merck (99%)), and citric acid (C<sub>6</sub>H<sub>8</sub>O<sub>7</sub>, Merck (99%)) were mixed

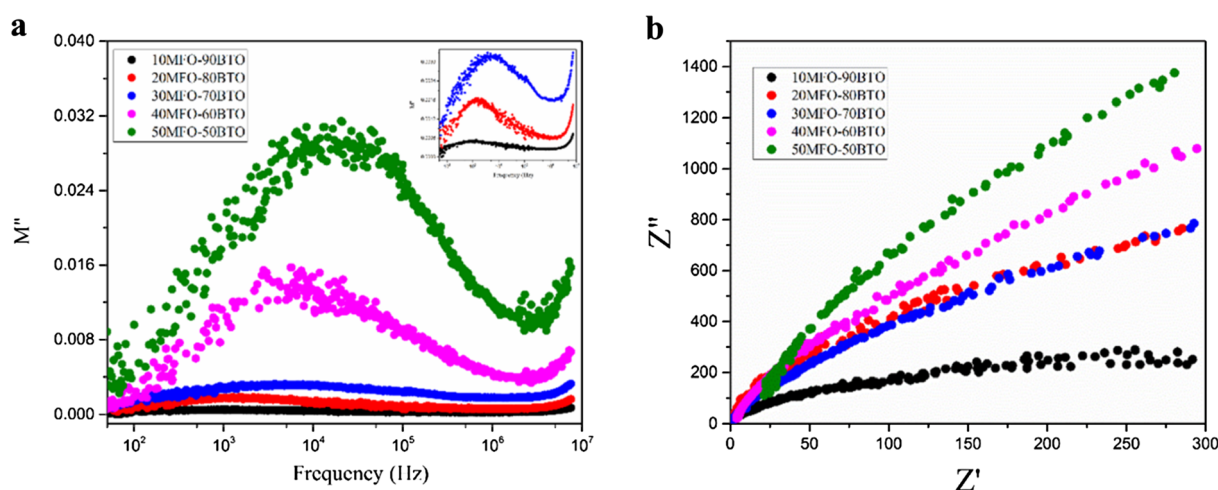


**Figure 8:** (a) Variation of the  $M''$  with frequency for (MFO)<sub>x</sub>–(BTO)<sub>(100–x)</sub> (x = 10, 20, 30, 40, 50) samples (inset shows the low frequency region for x = 10–30 samples). (b) Nyquist diagram ( $Z''$ – $Z'$ ) for studied samples.

in a 1:1 molar ratio of nitrate to citric acid to produce magnesium ferrite. Ammonia 25% solution ( $\text{NH}_3$ , Merck) was added drop by drop, while swirling continuously to get the pH to 7. While allowing the sol to evaporate, the temperature was kept at 150 °C. The viscosity went up as the concentration increased, and a gel started to form as a result of the crosslinking of carboxylate-metal complexes into a three-dimensional structure. The gel was instantly converted into nanocrystalline MFO powders after a sudden rise in temperature ( $T = 300$  °C). The reaction took 20 to 30 s to complete, producing a thick, dark gray substance. The BTO-MFO composites were made by combining the powders in different weight percentages with the formula  $(\text{MFO})_x-(\text{BTO})_{(100-x)}$  ( $x = 10, 20, 30, 40, 50$ ). The composite powders were then calcined for three hours at 1000 °C. After applying glue, PVA (polyvinyl acetate), it was compacted into round discs by uniaxial pressing. The resulting tablets were sintered for 2h at 1100 °C. The prepared samples were labeled 10MFO-90BTO, 20MFO-80BTO, 30MFO-70BTO, 40MFO-60BTO, and 50MFO-50BTO. Figure 1 shows a schematic representation of the preparation method for the BTO, MFO, and BTO-MFO nanocomposites.

## Funding

This work was supported by the Shahrood University of Technology.

## Data availability

The data is provided on request.

## Code availability

Not applicable.

## Declarations

**Conflicts of interest** There is no conflict of interest.

## References

1. M. Zolkepli, Z. Zainuddin, AIP Conference Proceedings, AIP Publishing LLC. 040014 (2015)
2. V. Naik, R. Mahendiran, Solid State Commun. **149**, 754–758 (2009)
3. M.M. Shirolkar, X. Dong, J. Li, S. Yin, M. Li, H. Wang, Phys. Chem. Chem. Phys. **18**, 25409–25420 (2016)
4. J. Allibe, S. Fusil, K. Bouzouane, C. Daumont, D. Sando, E. Jacquet, C. Deranlot, M. Bibes, A. Barthelemy, Nano Lett. **12**, 1141–1145 (2012)
5. B. Peng, Z. Zhou, T. Nan, G. Dong, M. Feng, Q. Yang, X. Wang, S. Zhao, D. Xian, Z.-D. Jiang, ACS Nano **11**, 4337–4345 (2017)
6. J.-M. Hu, T. Yang, J. Wang, H. Huang, J. Zhang, L.-Q. Chen, C.-W. Nan, Nano Lett. **15**, 616–622 (2015)
7. C. Rao, C.R. Serrao, J. Mater. Chem. **17**, 4931–4938 (2007)
8. S. Tan, S. Shannigrahi, S. Tan, F. Tay, J. Appl. Phys. **103**, 094105 (2008)
9. R. Tadi, Y.-I. Kim, D. Sarkar, C. Kim, K.-S. Ryu, J. Magn. Magn. Mater. **323**, 564–568 (2011)
10. A. Srinivas, R. Gopalan, V. Chandrasekharan, Solid State Commun. **149**, 367–370 (2009)
11. K. Singh, N. Negi, R. Kotnala, M. Singh, Solid State Commun. **148**, 18–21 (2008)
12. K. Sadhana, K. Praveena, S. Bharadwaj, S. Murthy, J. Alloy. Compd. **472**, 484–488 (2009)
13. M.V. Ramana, G. Sreenivasulu, N.R. Reddy, K.S. Kumar, B. Murthy, V. Murthy, J. Phys. D Appl. Phys. **40**, 7565 (2007)
14. S. Priya, R. Islam, S. Dong, D. Viehland, J. Electroceram. **19**, 149–166 (2007)
15. R.-F. Zhang, C.-Y. Deng, L. Ren, Z. Li, J.-P. Zhou, Mater. Res. Bull. **48**, 4100–4104 (2013)
16. L.N. Carter, C. Martin, P.J. Withers, M.M. Attallah, J. Alloy. Compd. **615**, 338–347 (2014)
17. L. Mitoseriu, V. Buscaglia, M. Viviani, M. Buscaglia, I. Palleschi, C. Harnagea, A. Testino, V. Trefiletti, P. Nanni, A. Siri, J. Eur. Ceram. Soc. **27**, 4379–4382 (2007)
18. A. Dzunuzovic, M.V. Petrovic, J. Bobic, N. Ilic, M. Ivanov, R. Grigalaitis, J. Banys, B. Stojanovic, Ceram. Int. **44**, 683–694 (2018)
19. H. Zheng, W. Weng, G. Han, P. Du, Ceram. Int. **41**, 1511–1519 (2015)
20. A. Guzu, C.E. Ciomaga, M. Airimioaei, L. Padurariu, L.P. Curecheriu, I. Dumitru, F. Gheorghiu, G. Stoian, M. Grigoras, N. Lupu, J. Alloy. Compd. **796**, 55–64 (2019)
21. M. Vijatović, J. Bobić, B. Stojanović, Sci. Sinter. **40**, 235–244 (2008)
22. E. Suharyadi, A. Hermawan, D. Puspitarum, Journal of Physics: Conference Series, IOP Publishing 2018, pp. 012003.
23. Q. Chen, A.J. Rondinone, B.C. Chakoumakos, Z.J. Zhang, J. Magn. Magn. Mater. **194**, 1–7 (1999)
24. R. Candeia, M. Souza, M.I.B. Bernardi, S. Maestrelli, I. Santos, A. Souza, E. Longo, Mater. Res. Bull. **41**, 183–190 (2006)
25. A. Pradeep, P. Priyadharsini, G. Chandrasekaran, J. Magn. Magn. Mater. **320**, 2774–2779 (2008)
26. S. Pradhan, S. Bid, M. Gateshki, V. Petkov, Mater. Chem. Phys. **93**, 224–230 (2005)
27. T. Sasaki, S. Ohara, T. Naka, J. Vejpravova, V. Sechovsky, M. Umetsu, S. Takami, B. Jeyadevan, T. Adschiri, J. Supercrit. Fluids **53**, 92–94 (2010)
28. I. Bergmann, V. Šepelák, K. Becker, Solid State Ionics **177**, 1865–1868 (2006)

29. S.V. Bangale, D. Patil, S. Bamane, Arch Appl Sci Res **3**, 506–513 (2011)
30. S. Verma, P. Joy, Y. Kholam, H. Potdar, S. Deshpande, Mater. Lett. **58**, 1092–1095 (2004)
31. A.R. Abraham, B. Raneesh, S. Joseph, P.M. Arif, P. Nambissan, D. Das, D. Rouxel, O.S. Oluwafemi, S. Thomas, N. Kalarikkal, Phys. Chem. Chem. Phys. **21**, 8709–8720 (2019)
32. R. Köferstein, T. Walther, D. Hesse, S.G. Ebbinghaus, J. Alloy. Compd. **638**, 141–147 (2015)
33. K. Verma, M. Singh, R. Kotnala, N. Goyal, J. Magn. Magn. Mater. **469**, 483–493 (2019)
34. S. Singh, N. Kumar, R. Bhargava, M. Sahni, K.-D. Sung, J. Jung, J. Alloy. Compd. **587**, 437–441 (2014)
35. P. Bongurala, V. Gorige, J. Magn. Magn. Mater. **477**, 350–355 (2019)
36. K.C. Verma, D. Singh, S. Kumar, R. Kotnala, J. Alloy. Compd. **709**, 344–355 (2017)
37. D. Fu, S. Hao, L. Qiang, J. Mater. Sci.: Mater. Electron. **24**, 1208–1212 (2013)
38. S.-S. Park, J.-H. Ha, H.N. Wadley, Integr. Ferroelectr. **95**, 251–259 (2007)
39. W. Fei, D. Xu, W. Li, L. Wang, W. Wang, Ferroelectrics **490**, 36–42 (2016)
40. R. Boddula, A.M. Asiri, Methods for Electrocatalysis: Advanced Materials and Allied Applications, Springer, (2020)
41. A.R. West, *Solid state chemistry and its applications* (John Wiley & Sons, Hoboken, 2022)
42. L. ElGendy, A. Ghani, A.S. Darwish, A. Sattar, Appl. Phys. A **127**, 1–14 (2021)
43. D. Sarkar, *Nanostructured ceramics: characterization and analysis* (CRC Press, Boca Raton, 2018)
44. A. Kheyrdan, H. Abdizadeh, A. Shakeri, M.R. Golobostanfard, J. Sol-Gel. Sci. Technol. **86**, 141–150 (2018)
45. Y. Slimani, N. Algarou, M. Almessiere, A. Sadaqat, M. Vakhtov, D. Klygach, D. Tishkevich, A. Trukhanov, S. Güner, A. Hakeem, Arab. J. Chem. **14**, 102992 (2021)
46. S.K. Durrani, S. Naz, M. Mehmood, M. Nadeem, M. Siddique, J. Saudi Chem. Soc. **21**, 899–910 (2017)
47. P. Demircivi, B. Gulen, E.B. Simsek, D. Berek, Mater. Chem. Phys. **241**, 122236 (2020)
48. Z. Charifi, H. Baaziz, N. Bouarissa, Int. J. Mod. Phys. B **18**, 137–142 (2004)
49. A.R. Abraham, B. Raneesh, D. Das, N. Kalarikkal, AIP Conference Proceedings, AIP Publishing LLC, 050151, (2016)
50. Y. Peng, C. Xia, M. Cui, Z. Yao, X. Yi, Ultrason. Sonochem. **71**, 105369 (2021)
51. M. Almessiere, Y. Slimani, M. Sertkol, M. Nawaz, A. Baykal, I. Ercan, Results Phys. **13**, 102244 (2019)
52. M.V. Shisode, D.N. Bhojar, P.P. Khirade, K. Jadhav, J. Supercond. Novel Magn. **31**, 2501–2509 (2018)
53. U. Khan, N. Adeela, K. Javed, S. Riaz, H. Ali, M. Iqbal, X. Han, S. Naseem, J. Nanopart. Res. **17**, 1–9 (2015)
54. V. Banihashemi, M. Ghazi, M. Izadifard, J. Mater. Sci.: Mater. Electron. **30**, 17374–17381 (2019)
55. L.J. Berchmans, R.K. Selvan, P.S. Kumar, C. Augustin, J. Magn. Magn. Mater. **279**, 103–110 (2004)
56. L. Solymar, D. Walsh, R.R. Syms, *Electrical properties of materials* (Oxford University Press, Oxford, 2014)
57. M. Naeem, N.A. Shah, I.H. Gul, A. Maqsood, J. Alloy. Compd. **487**, 739–743 (2009)
58. R. Devan, S. Lokare, D. Patil, S. Chougule, Y. Kolekar, B. Chougule, J. Phys. Chem. Solids **67**, 1524–1530 (2006)
59. D.R. Uhlmann, G. Teowee, J. Boulton, J. Non-Cryst. Solids **131**, 1194–1201 (1991)
60. R. Tadi, Y.-I. Kim, C.-G. Kim, K.-S. Ryu, Proceedings of the Korean Magnetics Society Conference, The Korean Magnetics Society2011, pp. 93–95.
61. Y. Zhang, T. Pan, Z. Yang, Chem. Eng. J. **389**, 124433 (2020)
62. G. Nasr, R. Ahmed, Mod. Phys. Lett. B **24**, 911–919 (2010)
63. C. Wang, H. Gao, D. Liang, S. Liu, H. Zhang, H. Guan, Y. Wu, Y. Zhang, Adv. Compos. Hybrid Mater. **5**, 2906–2920 (2022)
64. H. Gao, C. Wang, Z. Yang, Y. Zhang, Compos. Sci. Technol. **213**, 108896 (2021)
65. R. Mangalaraja, P. Manohar, F. Gnanam, M. Awano, J. Mater. Sci. **39**, 2037–2042 (2004)
66. S.F. Chérif, A. Cherif, W. Dridi, M.F. Zid, Arab. J. Chem. **13**, 5627–5638 (2020)
67. S. Shankar, O. Thakur, M. Jayasimhadri, Mater. Chem. Phys. **234**, 110–121 (2019)
68. S. Sharma, T. Basu, A. Shahee, K. Singh, N. Lalla, E. Sampathkumar, J. Alloy. Compd. **663**, 289–294 (2016)
69. A.B. Abou Hammad, A.G. Darwish, A.M. El Nahrawy, Appl. Phys. A **126**, 1–12 (2020)
70. M. Mojahed, H.R. Dizaji, A. Gholizadeh, Phys. B **646**, 414337 (2022)

**Publisher's Note** Springer Nature remains neutral with regard to jurisdictional claims in published maps and institutional affiliations.

Springer Nature or its licensor (e.g. a society or other partner) holds exclusive rights to this article under a publishing agreement with the author(s) or other rightsholder(s); author self-archiving of the accepted manuscript version of this article is solely governed by the terms of such publishing agreement and applicable law.